Exp Fluids (2011) 51:407–421
DOI 10.1007/s00348-011-1039-9

RESEARCH ARTICLE

Comparison of velocity and temperature measurements with simulations in a hypersonic wake flow

Robert Hruschka · Sean O'Byrne · Harald Kleine

Received: 9 May 2010 / Revised: 30 November 2010 / Accepted: 3 January 2011 / Published online: 1 March 2011

Abstract A hypersonic shock-tunnel flow around an axisymmetric model of a planetary entry probe is analyzed. Planar laser-induced fluorescence is applied to measure both the velocity and the rotational temperature everywhere in the central plane of the flow field. The experimental test case is compared to simulations using the direct simulation Monte Carlo (DSMC) method. While the Mach 9.7 flow at a freestream Reynolds number based on the model diameter of 35,000 is chemically frozen, effects of thermal non-equilibrium and localized rarefaction cannot be neglected. DSMC and measurements agree well within the outer wake, but disagree close to the centerline, where in particular the measured velocity is higher than values predicted by the simulations. The experimental results indicated a shorter recirculation region and increased local fluctuations in the free shear layer upstream of the wake recompression shock when compared to the simulation. These effects are attributed to incipient transition, which is not observed in the simulations, as the simulations did not model the effects of freestream fluctuations. Furthermore, measured and simulated vorticities are compared with theoretical predictions.

1 Introduction

Modern interplanetary space exploration missions mostly rely on aerobraking maneuvers at high speeds to slow down space vehicles upon entry into a planetary atmosphere. Therefore, it is important to analyze the hypersonic flow fields experienced by these probes, shown schematically in Fig. 1. The design of surface heating protection, payload distribution, and aerodynamic stability are governed by the nature of these flows. Simulations are challenged not only by the complexity of these flows but also by the interaction of hypersonic real gas effects, like chemical reactions (Dogra et al. 1995), ionization (Ozawa 2008), radiative coupling (McIntyre et al. 2009; Sohn et al. 2009), and thermal non-equilibrium (Zhong et al. 2008). In addition, high-altitude flows are most likely affected by localized rarefaction effects (Bird 1994), which cause systematic error in results obtained using Navier-Stokes (NS)-based numerical simulation schemes (Lofthouse et al. 2007). In lower-altitude, higher-density flows, the onset of turbulence occurs first in the wake far downstream of the body and moves closer to the rear stagnation point as the vehicle descends and the flow density increases (Lees1964). The gradual increase in transient non-linear disturbances with increasing base distance eventually leads to full transition further downstream in the flow (Behrens1968). Modeling this phenomenon poses formidable challenges to simulations, as velocity variations in the freestream and surface imperfections can cause unstable oscillation modes to be amplified (Hornung and Lemieux 2001). If the wake flow field is investigated in a shock tunnel, the flow noise produced by such a facility can influence the location of transition from laminar to turbulent behavior (Schneider 2001). Prediction of this transition is very difficult to achieve accurately with NS-based flow computations, and most of these computations tend to assume either fully laminar or fully turbulent flow. Hypersonic near-wake flows are problematic in this regard due to the tendency of these flows to undergo transition in the shear layer. While Liou et al. (1993) have shown that direct simulation Monte Carlo (DSMC) (Bird 1994) methods are capable of simulating the

R. Hruschka (✉) · S. O'Byrne · H. Kleine
School of Engineering and Information Technology, University of New South Wales, Australian Defence Force Academy, Canberra, ACT 2600, Australia
e-mail: r.hruschka@adfa.edu.au

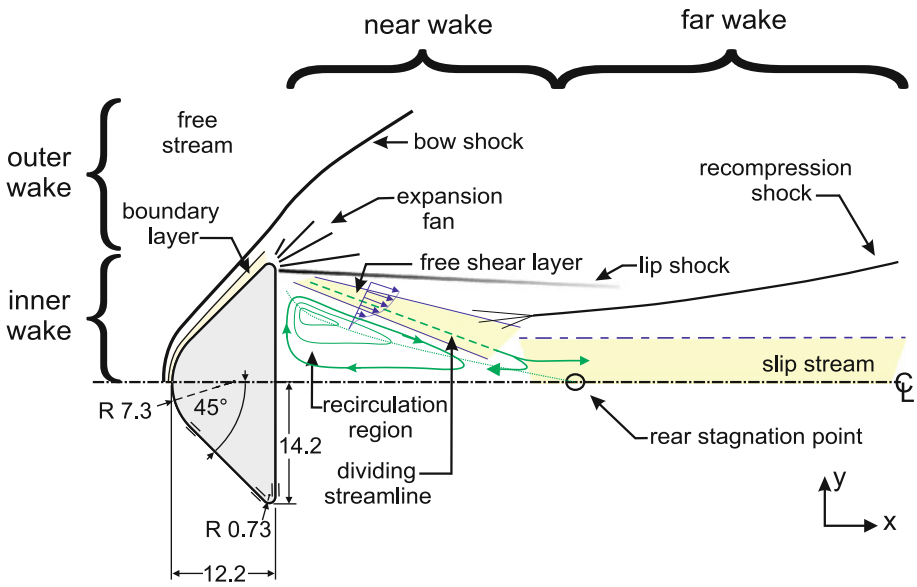

Fig. 1 Schematic of a hypersonic wake flow and dimensions of the used model in millimeters

formation of the three-dimensional structures that are thought to precede transition, the technique's ability to predict transition phenomena has not been demonstrated.

DSMC has considerably advanced numerical work on low-density entry flows, as current computational resources allow the method to be used to validate scaled measurements conducted in hypersonic facilities at global Knudsen numbers (Kn_d) less than 10^{-3} (Moss and Bird 2005). The agreement of DSMC simulations of representative planetary entry flows in wind tunnels with measured data is generally better than the agreement of NS-based simulations (Moss and Price 1997; Zhong et al. 2008), as the DSMC method is unaffected by the breakdown of continuum assumptions (Boyd 1995). Unlike NS-based simulations, DSMC simulates internal shock structures directly (Schwarzentruber et al. 2008) and does not require additional imposed boundary conditions to model surface velocity slip and temperature jump (Inger and Moss 2007).

Despite these advances in simulation capability, the complexity of hypersonic flows warrants experimental validation of simulations. Accurate measurements of flow field parameters in model planetary entry flows, however, are comparatively rare. Murman (1969), for example, measured the pitot pressure field behind a magnetically suspended slender cone in a Mach 16 tunnel flow and inferred local flow velocities from these measurements. The pitot probe used, however, was not sensitive enough to map the velocity field within the recirculation region, which is easily disturbed by such an intrusion, as described by Zakkay and Cresci (1966). Zhong et al. (2008) simulated Murman's flow field and found that the velocity deficit in the far wake three base diameters downstream of the model was about 50% higher than the measured deficit. The measurements and simulations of number flux behind a wire-mounted blunted cone at Mach 16 by Danckert and Legge (1996) were different by only 20% two model diameters downstream of the base, however at a global Knudsen number about an order of magnitude larger than the current Kn_d, which supports the assumption of fully laminar flow made in ref. (Danckert and Legge (1996). Using electron beam fluorescence to measure the temperature at the centerline behind wire-mounted, slightly blunted cones in Mach 12.6 to 17.9 flows, Muntz and Softley (1996) found distinct peak temperatures in the vicinity of the rear stagnation point, with the effect being most emphasized at the lowest Re_d of 5×10^4, which is of the same order as Re_d in the current investigation. Todisco and Pallone (1965) used hot-wire probes to measure the stagnation temperature along the centerline of a sharp cone wake flow at Mach 16, which agreed well with the simulations of (Zhong et al. 2008) in the far wake, but showed discrepancies of up to 30% in the recirculation region. Due to the use of different techniques, some of which could have caused flow disturbance, and also different tendencies to show first signs of turbulence in the flow fields investigated, it is difficult to obtain a general picture of the relevant processes in the inner wake close to the base from existing studies. Hence, the current study was conducted to obtain a complete data set of velocity (Hruschka et al.2010) and temperature for a hypersonic wake flow that can be directly compared to simulations. This was achieved by using a non-intrusive optical technique and minimizing the influence of mounting structures (Hruschka et al. 2009).

2 Hypersonic flow properties and model dimensions

The measurements were conducted in the T-ADFA free-piston shock tunnel facility (Gai 1992; Hruschka et al.2010). To determine the nozzle inlet conditions at the time of the measurement, the shock-heated reservoir gas conditions were measured and are listed in Table 1. A time history of the measured reservoir pressure is shown in Fig. 2. The reservoir temperature was determined from this pressure and the measured shock speed using the one-dimensional shock tube code ESTC (McIntosh 1968). The reservoir feeds a conically diverging nozzle with a throat diameter of 12.7 mm, a length of 1,110 mm, and an exit diameter of 305 mm. This results in a diverging test flow, and the flow parameters depend on the distance downstream of the nozzle exit. A one-dimensional non-equilibrium nozzle code (O'Byrne et al. 2006) was used to calculate the freestream parameters, which are listed in Table 2. The calculated pitot pressure was matched to the measured value, also shown in Fig. 2, by changing the effective nozzle angle in the code, in order to account for the displacement thickness of the nozzle boundary layer. This semi-empirical method of calculating freestream parameters generally agrees with measurements to within 5% (O'Byrne 2002). The calculated freestream parameters and their gradients in the flow direction due to the flow divergence are listed in Table 2. Within the steady flow period, indicated in Fig. 2, the pitot pressure changes by less than 8%. The Reynolds number Re_d and the Mach number M are based on the transrotational temperature.

Table 1 Nozzle reservoir conditions with standard deviations (STD), indicating the variations between facility runs

Parameter	Unit	Value	STD (%)
Initial fill pressure	[Pa]	66×10^3	(0.2)
Incident shock speed	[m/s]	1,935	(0.6)
Reservoir temperature	[K]	3,051	(1.0)
Reservoir pressure	[Pa]	11.5×10^6	(2.6)

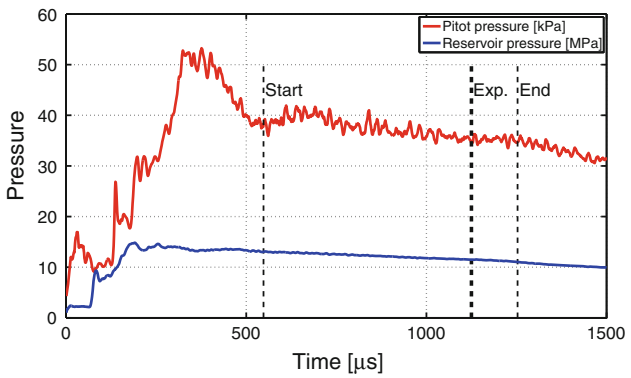

Fig. 2 Measured pressure histories of the T-ADFA shock tunnel. Start and end of steady flow period and the time of the measurement (Exp.) are marked

Table 2 Freestream conditions at the model tip (15 mm downstream of nozzle exit) with gradients in flow direction

Parameter	Unit	Value	Gradient (m^{-1})
Trans./rot. temp.	[K]	165	−108
Vib. temp. (N_2)	[K]	2,390	0
Vib. temp. (O_2)	[K]	1,270	0
Vib. temp. (NO)	[K]	340	0
Density	[kg/m^3]	0.006	−0.0097
Axial (x) velocity	[m/s]	2,503	43
Radial (y) velocity	[m/s]	2,058	−1,596
Reynolds No. (Re_d)	[–]	35,000	−43,000
Mach No. (M)	[–]	9.7	3.5

Calculated species mole fractions within the flow: 77% N_2, 18% O_2, 5% NO. The radial velocity component increases proportionally with the radial coordinate y and is given at $y = 1$ m

The model used in this work features a 1:12.32 scaled version of the forebody of the Mars Microprobe (Gnoffo 1999; Mitcheltree et al. 1999) with a diameter d of 28.4 mm and a flat base. The model dimensions are given in Fig. 1. Four 0.2-mm-diameter steel wires were used to hold the model in place. Time-resolved visualizations have shown that these wires cause only localized and insignificant flow disturbances in the wake when compared to a free-flying model (Hruschka et al. 2009). A large aspect ratio of about seven between the nozzle inviscid core flow and the model diameter was chosen to avoid interferences by the expansion fan originating from the nozzle exit on the near-wake flow.

3 Simulations of the flow field

The DSMC method simulates collisions between individual molecules in a probabilistic manner. Typically, a single simulated molecule represents a much larger number of real molecules in the flow. Collisions and particle motion are temporally decoupled and are simulated alternately, at numerical time steps smaller than the mean time between collisions. The macroscopic flow properties of interest are sampled from a usually small number of microscopic particles, which leads to statistical scatter larger than in the real flow.

The axisymmetric tunnel flow field around the planetary entry probe model has been simulated with the DSMC code DS2V (Bird 2007), developed by Bird (1994). Similar to previous numerical studies on planetary entry type flows (Dogra et al.1995; Moss 2007; Zhong et al. 2008), the variable hard sphere (VHS) model was used. This implies that the dynamic viscosity μ has a dependence on

temperature T of the form $\mu = \mu_{ref}(T/T_{ref})^{\omega}$. The molecular diameter d of each species is a function of the relative velocity c_r in the collision and can be determined from reference values (Bird 1994):

$$d = d_{ref}\left[\left(\frac{2k_B T_{ref}}{m_r c_r^2}\right)^{\omega-0.5}\cdot\frac{1}{\Gamma(5/2-\omega)}\right]^{0.5}, \quad (1)$$

where k_B is the Boltzmann constant and m_r the reduced mass of the collision pair. Values for the molecular reference diameter d_{ref} at reference temperature $T_{ref} = 273$K, the molecular mass m and the viscosity-temperature exponent ω are listed in Table 3. DS2V models a translational, rotational, and a vibrational temperature for each species. The code uses a quantum-based Larsen–Borgnakke model (1975), to simulate the exchange of internal energy between these modes. While the rotational relaxation number Z_{rot} was modeled independently of temperature, temperature-dependent vibrational collision numbers Z_{vib} were calculated using Eq. 6.53 in Ref. (Bird 1994). Reference values for Z_{vib} at the characteristic vibrational temperature Θ_{vib} are given in Table 3.

Dissociation was also modeled, based on the characteristic dissociation temperature Θ_D (Bird 1994). At a stagnation enthalpy of 3.8 MJ/kg, however, atomic oxygen was found at the concentrations of less than 0.1%, and therefore, the flow field can be considered as chemically frozen. Diffuse molecular reflection from the model surface at 300 K was assumed. The modeling of vibrational relaxation during surface collisions can influence surface heat flux. Simulating thermal accommodation of both rotational and vibrational energy to surface values, Moss and Bird (2005) found that the surface heat flux on a cone in hypersonic flow was 5–10% high with respect to a simulation where only the rotational energy was accommodated. The full surface accommodation, however, showed better agreement with measurements. As the current tunnel freestream is similar to one of the conditions investigated by Moss and Bird (2005), full surface accommodation was also assumed in the current work. The modeling of vibrational surface relaxation, however, has less influence on flow field velocity and temperature than it has on surface heat flux: simulating only rotational accommodation at the surface of the current model led to changes in these values of less than 3% in the wake.

Table 3 Molecular parameter values for the species occurring in the current flow field

Parameter	Unit	N_2	O_2	NO
Mol. mass (m)	[kg]	4.65×10^{-26}	5.312×10^{-26}	4.98×10^{-26}
Mol. ref. ϕ (d_{ref})	[m]	4.17×10^{-10}	4.07×10^{-10}	4.20×10^{-10}
$\mu - T$ exponent (ω)	[–]	0.74	0.77	0.79
Rot. coll. No. (Z_{rot})	[K]	5	5	5
Vib. temp. (Θ_{vib})	[K]	3,371	2,256	2,719
Vib. coll. No. (Z_{vib})	[K]	52,500	17,900	1,400
Diss. temp. (Θ_D)	[K]	11,3500	59,500	75,500

Reference temperature for $d_{\text{ref}} = 273$ K. Reference temperature for $Z_{\text{vib}} = \Theta_{\text{vib}}$. The data has been adopted from (Bird 1994), also implemented in DS2V (Bird 2007)

The quality of a DSMC simulation is primarily determined by the value of the ratio of the simulated mean collision separation to the physical mean free path (MCS/MFP), which should be smaller than unity everywhere in the flow field (Bird 1994). For the current simulation, this parameter was smaller than 0.1 for most of the flow field, with a peak value of 0.4 in the forebody flow. Starting with a low number of simulated molecules, the simulation was run until the flow field had reached steady state. Then, the number of molecules was approximately doubled, both collisional and sampling grids were refined and the sampling of flow field parameters restarted. This procedure was repeated until none of the parameters changed by more than 2%. The dependence of selected parameters on the number of simulated molecules is illustrated in Fig. 3. Numerical independence of forebody heat flux required approximately 4×10^7 molecules to be simulated; however, other parameters required fewer simulated molecules. Including the effect of statistical scatter inherent to the DSMC method, the simulation results using 9.7×10^7 particles discussed in the following sections are numerically accurate to within 2%, based on the observed changes relative to a simulation using only 6.5×10^7 particles.

The calculated tunnel freestream parameters listed in Table 2 were used for the DSMC simulation, including the flow divergence and the individual species-specific

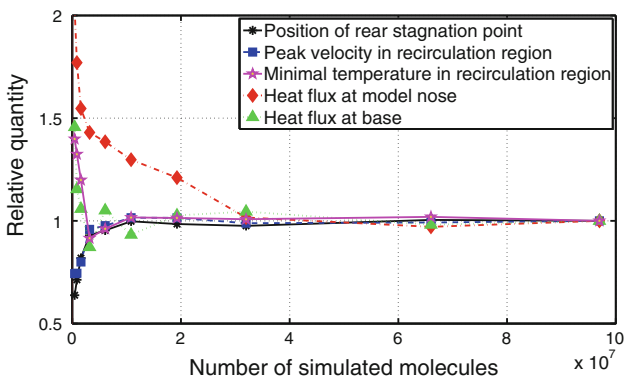

Fig. 3 Dependence of selected parameters on the number of simulated particles, relative to the final result using 9.7×10^7 particles

temperature modes. Flow imperfections in the freestream, however, were not modeled, as these fluctuations could not be quantified. Slight unsteadiness of the shock waves, i.e. fluctuation magnitudes with a standard deviation equivalent to about 2% of the model diameter were observed in time-resolved visualizations of the flow field (Hruschka et al. 2009), which indicate the presence of such imperfections.

4 Thermal non-equilibrium and rarefaction effects

The simulations allow the effect of thermal non-equilibrium between vibrational (T_{vib}) and translational temperatures (T_{tr}) on the wake to be analyzed. The top half of Fig. 4 shows a non-equilibrium parameter, defined as T_{vib}/T_{tr}, where T_{vib} is an averaged value weighted by the concentrations of the individual species, as listed in Table 2. The vibrationally excited freestream, typical for shock tunnel flows of air (Ruffin 1993; O'Byrne et al. 2006), comes to equilibrium when passing through the bow shock close to the centerline. Further away from the centerline, however, this vibrational relaxation occurs only partially, as the shock becomes weaker. When the boundary layer separates from the model, T_{tr} drops rapidly, whereas T_{vib} freezes in the strong corner expansion, which is typical for hypersonic blunt-body flows (Zhong et al. 2008). In the inner wake, only a small degree of non-equilibrium is observed. To further investigate the impact of thermal non-equilibrium on the chemically frozen wake flow, a second "equilibrium" simulation modeling instantaneous relaxation ($Z_{vib} = 1$) is performed, and the results are compared with experiments in Sect. 6.

This wake flow also experiences some effects of flow rarefaction. For example, a small shock in the recirculation region, where the upstream-directed flow at the centerline decelerates from slightly supersonic Mach numbers, can be clearly observed as a density discontinuity in Navier-Stokes (NS)-based simulations of the flow (Hruschka 2010), but is not apparent in the DSMC simulations or the experiments. This indicates that this flow feature is most likely an artifact created in the NS-based simulations and probably caused by localized continuum breakdown. To characterize the degree of this continuum breakdown, which also renders the NS no-slip boundary condition locally invalid (Bird 1994; Shen 2005) and can therefore cause simulation errors in hypersonic wakes (Lofthouse et al. 2008), Boyd et al. (1995) have introduced the local gradient-length Knudsen number, Kn_{GLL}, defined as:

$$Kn_{GLL} = \frac{\lambda_m}{Q}\left(\frac{\partial Q}{\partial l}\right), \tag{2}$$

where λ_m is the molecular mean free path, Q a flow parameter, and l a length coordinate in the direction of the strongest gradient of Q. The Kn_{GLL}-field, using the static pressure p for Q, is plotted in the bottom half of Fig. 4, where the regions of large values are highlighted. Rotational and translational temperatures for each species were found to be in equilibrium, except in regions where Kn_{GLL} exceeds 0.02. In those regions, differences were typically in the order of 5%. Furthermore, surface velocity slip (Lofthouse et al. 2008) of the order of 8% of the freestream velocity occurs locally at the separation location. This suggests that the DSMC method is more suitable to model this particular flow field than NS-based simulations, as otherwise some systematic error due to continuum breakdown could occur, as also emphasized by Moss and Price (1997) or Lofthouse et al. (2007) for flows at similar or slightly higher global Knudsen numbers.

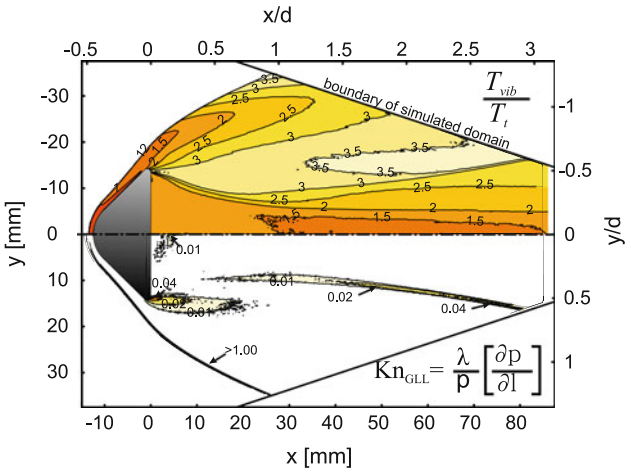

Fig. 4 Simulated local degree of vibrational non-equilibrium (*top*) and degree of flow rarefaction (*bottom*)

5 Experimental measurements

The velocities in both axial and radial directions and the rotational temperatures were measured everywhere in a central plane through the flow axis. Multiple measurements of pulsed planar laser-induced fluorescence (PLIF) of nitric oxide (NO) (McMillin 1993; Eckbreth 1996) were obtained over several shock tunnel runs, each measurement requiring a separate tunnel run. The measured velocities and temperatures were averaged over the facility runs, and the uncertainty in these parameters depends mainly on the local steadiness of the flow. Locally unsteady flow can therefore be identified by increased uncertainty, with unsteady flow regions characterized by greater variability in fluorescence signal from one facility run to the next. A completely established wake flow was assured by analyzing the time-dependent behavior of the velocity-sensitive

fluorescence distribution at the flow centerline (Hruschka et al. 2010).

5.1 Velocity measurements

The velocity field was obtained by measuring Doppler shifts in the center plane in directions parallel and perpendicular to the flow. Similar to the concept demonstrated by Danehy et al. (2001), a UV laser was scanned in discrete steps over an isolated spectral line within the $\gamma(0,0)$ band of nitric oxide, which is formed during the reflection of the shock wave in the nozzle reservoir. The velocity field measurement and the diagnostic system arrangement used is described in detail in Ref. (Hruschka et al. 2010). Fitting the line shape function to the individual fluorescence measurements allowed both line shape and center to be determined. In the low-density hypersonic wake flow field, spectral lines experience primarily Doppler shifts proportional to the local bulk velocity of the flow. If these shifts are in the direction of the fluorescence-exciting laser sheet, the spectral line appears displaced from its vacuum center location. These Doppler shifts were used to infer the local flow velocity and its vector field. About 60 tunnel runs were required to determine the shifted line center everywhere in the flow. The resulting time- and run-averaged velocity measurement is shown in the top half of Fig. 5 for the radial and Fig. 6 for the axial velocity component.

As mentioned above, the magnitude of the averaged velocity uncertainty serves as an indicator of both variability in the technique and local flow steadiness and repeatability. The contribution to the variability from the measurement system is nearly the same everywhere in the flow, while larger localized signal variations can be attributed to variability in the flow. The background

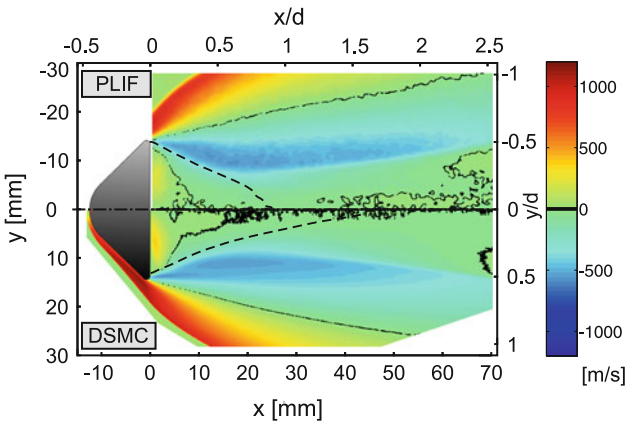

Fig. 5 Comparison of measured (*top*) and simulated (*bottom*) *radial* velocity component. Regions where the radial velocity component is zero are *marked black*. The dividing streamline is indicated as a *black*, *dashed line*

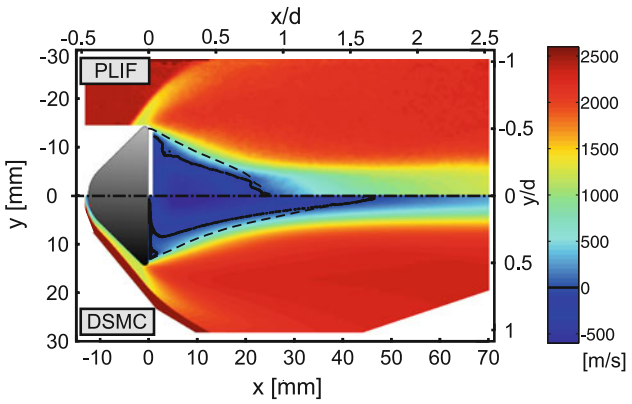

Fig. 6 Comparison of measured (*top*) and simulated (*bottom*) *axial* velocity component. Regions of zero axial velocity are *marked black*. The dividing streamline is indicated as a *black*, *dashed line*

velocity uncertainties were typically within 95% confidence intervals of 50 m/s, except in a region at the outer radius of the slipstream at $y/d \approx 0.2$, where the uncertainty could be as high as 150 m/s due to the presence of local velocity variability (Hruschka et al. 2010).

Pressure shifts, laser attenuation, and motion blur due to the finite camera gating time can cause systematic error in the velocity measurement. Motion blur is only significant immediately behind the bow shock, where the effects could extend as far as 1.7% of the model diameter downstream of the shock. Elsewhere in the flow, both velocities and their gradients are too small to cause significant error. The systematic error due to laser-wavelength-dependent laser-sheet attenuation, as described in (Hruschka et al. 2010), was found to be well below random uncertainties by comparison of different measurements, and hence unmeasurable. The calculated systematic error caused by the pressure shift is below 10 m/s nearly everywhere in the flow field, but can exceed the random error of ±50 m/s at the bow shock and up to 2 mm immediately downstream of it (Hruschka et al. 2010).

5.2 Temperature measurements

Rotational PLIF two-line thermometry (McMillin 1993) takes advantage of the temperature dependence of the population distribution of different rotational ground states. Two NO lines within the same vibrational band with a large rotational energy separation are each probed successively with the PLIF laser. If the rotational state populations follow a Boltzmann distribution, the ratio of the two fluorescence signals can be used to determine the rotational temperature:

$$T_{rot} = \frac{E_{R,2} - E_{R,1}}{k_B ln\left(\frac{B_{12,2}(2J_2+1)F_1}{B_{12,1}(2J_1+1)F_2}\right)} \quad (3)$$

where $E_{R,2}$ and $E_{R,1}$ are the ground-state (rotational) energies, J_2 and J_1 the rotational quantum numbers, and $B_{12,2}$ and $B_{12,1}$ the Einstein coefficients for stimulated absorption of the two probed lines, respectively. The terms F_2 and F_1 are the recorded fluorescence intensities, averaged over multiple tunnel runs, and corrected for energy fluctuations of the exciting laser and camera dark noise (Hruschka et al. 2010).

The ${}^{R}R_{22}(14)$ and the ${}^{P}P_{11}(26)$ lines within the NO $\gamma(0,0)$ band probed in this work were found to be a good compromise between low laser-sheet attenuation, acceptable signal-to-noise ratio, and large energy separation. Both lines share the same electronic and vibrational states, and thus, the Einstein B coefficients can be substituted by purely rotational line strength factors, known as Hönl-London factors (H_L). Expressions for calculating H_L values are given in Ref. (Earls 1935), and their values for the two lines used here are listed in Table 4.

Both lines were probed several times to obtain the time-averaged temperature field. To reduce the influence of pixel noise, which could otherwise lead to systematic error due to the non-linear relationship between the ratio of the two fluorescence signals and the temperature (Houwing et al. 1996), the top and bottom halves of several fluorescence images were combined as an average and smoothed within 5 × 5 pixels, which corresponds to 3% of the body diameter. The temperatures determined using Eq. 3 have 95% confidence intervals of ±70–150 K for most of the flow field, except in the region of the slipstream downstream of reattachment and immediately behind the bow shock, where uncertainties were found to be about twice as high. The increased uncertainty within the slipstream is attributed to unsteady flow in this region, causing larger run-to-run variations in the averaged fluorescence signals and hence increased temperature uncertainty. Immediately behind the bow shock, where the temperatures are approximately 1,600 K, the temperature is particularly sensitive to changes in the ratio of the two fluorescence signals; hence, the susceptibility to random uncertainty becomes larger (Seitzman and Hanson 1993).

Systematic error in temperature measurements results if the ratio of the two required fluorescence intensities, F_1 and F_2, becomes biased. This can occur if one of the two lines *a*), causes stronger absorption of the laser or *b*), experiences a higher level of saturation compared to the other probed line. Saturation, or depletion of the lower laser-coupled quantum state (Demtröder 1999), can be avoided by choosing lines with similar Hönl-London factors, or reducing the laser intensity well below the saturation intensity (Seitzman and Hanson 1993). Both strategies were followed in the current work, ensuring that systematic error due to saturation stays below 3% throughout the flow field.

Table 4 Parameters of the two probed lines within NO $A^2\Sigma^+ \leftarrow X^2\Pi$ ($v'' = 0$)

Line	Index	E_R	J	H_L
${}^{R}R_{22}(14)$	1	394.9 cm^{-1}	13.5	0.314
${}^{P}P_{11}(26)$	2	1156.2 cm^{-1}	26.5	0.402

The symmetry of the flow field was exploited to determine the degree of laser-sheet absorption, specifically by monitoring the laser intensity before and after the laser had propagated through the absorbing parts of the flow. The freestream itself absorbs only weakly, so the spatially homogeneous fluorescence signal in this region can be used as an intensity reference. Probing the ${}^{R}R_{22}(14)$ line, the freestream fluorescence was 14.8% low in the bottom-half freestream region, compared to the corresponding signal in the top half. This indicated that the laser sheet, entering from the top, had been attenuated by the same amount. The average attenuation in the averaged half-image hence becomes 7.4%, for which the intensity F_1 was corrected before calculating the temperatures. The lower absorption cross-sections of the ${}^{P}P_{11}(26)$ line due to smaller thermal populations caused negligible absorption of the F_2-signal. If the attenuation of the F_1-signal was not considered, the temperatures would have been typically ≈5% high, with peak values of systematic error reaching ≈13% in the hot regions immediately behind the bow shock (Hruschka 2010). The only region where the temperature was low enough to cause significant uncertainty in the F_2-signal was the freestream. For this reason, the measured freestream temperature of 220 ± 100 K has higher relative uncertainty than other flow regions.

6 Comparison of measurement and simulation

Measurements and simulations agreed exceptionally well in the outer wake, at radii larger than approximately 0.25 model diameters, where the flow can be considered inviscid (Lees 1964). Discrepancies in the temperature and velocity distributions were found, however, at smaller radial distances. These discrepancies could not be explained by either measurement or simulation uncertainty. The measured freestream velocity of 2,410 ± 50 m/s is 3.5% low compared to the value calculated using the 1-D nozzle code, listed in Table 2. This is similar to the findings of Beck (1999), Danehy et al. (2003), and O'Byrne (2002) and suggests that the commonly used semi-empirical method to calculate hypersonic shock tunnel freestream conditions tends to overpredict the nozzle-exit velocity. Considering the large uncertainty of the measured trans-rotational freestream temperature, a comparison is difficult.

The influence of a freestream temperature systematically high by 55 K has, however, only a minor influence on stagnation enthalpy (≈1%), which governs most of the properties of the hypersonic wake of blunt bodies (Dewey 1965; Reeves 1965).

6.1 Velocity

Comparisons between measured and simulated radial (y) and axial (x) velocity components are shown in Fig. 5 and Fig. 6, respectively. The radial velocity component agrees well with simulations everywhere in the wake, except close to the base at $x \approx 2$ mm, where the radially outwards directed flow is about 30% slower than simulated, indicating a lower rotation speed of the vortices within the recirculation zone. More detail can be observed in Fig. 7a, b, which show the radial velocity distribution in the near wake at $x/d = 0.25$ and in the far wake at $x/d = 2$, respectively. Some discrepancy is observed at $x/d = 0.25$ and $y/d \approx 0.9$, where the simulated velocity jump across the bow shock occurs more suddenly than in the experimental case. The primary reasons for this discrepancy are the uncertainty due to motion blur of the camera system (Hruschka et al. 2010) and local unsteadiness of the bow shock of about 2% of the model diameter (Hruschka et al. 2009). The effect of these uncertainties on the velocity is indicated by a horizontal error bar. At $x/d = 2$ and $y/d \approx 0.4$ (Fig. 7b), the measured velocity jump across the recompression shock occurs at a slightly smaller radial distance than simulated. The discrepancy can be reduced by adjusting the freestream velocity of the simulation to the measured value.

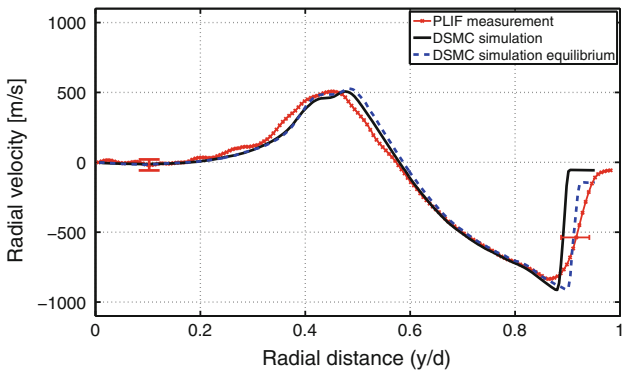

(a) Radial velocity at x/d=0.25

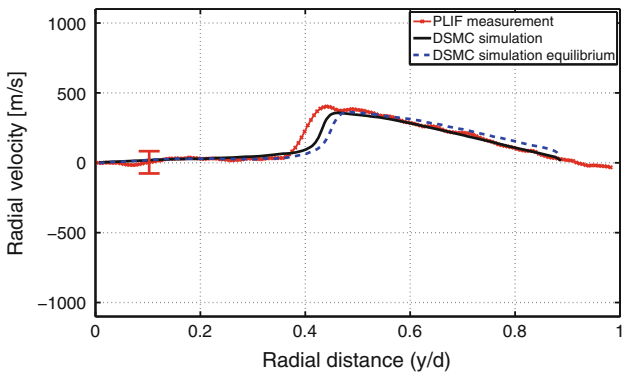

(b) Radial velocity at x/d=2

Fig. 7 Comparison of radial velocities in the near and far wake, DSMC and PLIF

The axial velocity comparison (Fig. 6) also shows agreement in the outer wake, but measurements and simulations do not agree in the inner wake, at $y/d < 0.2$. The discrepancy becomes particularly obvious at the location of the indicated zero velocity line, and the far wake downstream of it. Within the recirculation region, lower velocities are observed in the experimental data compared with the simulated velocity. These differences are most likely linked to the larger discrepancies evident further downstream. The simulations indicate gradual velocity recovery with distance from the base at the centerline, as shown in Fig. 8, whereas the experiments indicate that the velocity at the centerline regains the velocity of the outer inviscid stream much more rapidly. Figure 9a, b show the axial velocity distribution in the near and far wake measured at $x/d = 0.25$ and $x/d = 2.0$ and along radial distance (y/d). Below each plot, the uncertainty of the measured velocity magnitude is shown. Both plots show the measured velocity about 5% lower than simulated in the outer wake. This discrepancy is caused by the systematically high freestream velocity calculated by the nozzle code and did not occur in another simulation where the inlet velocity of the simulation was adjusted to the lower measured value. The axial location of the peak reverse flow velocity is $x/d = 0.25$, and its measured value of 492 ± 50 m/s is approximately 20% lower than the simulated value of 612 m/s. This difference cannot be removed by adjusting the simulated freestream velocity, but is reduced to approximately 15%. The discrepancy between measured and simulated axial velocities, however, is much larger further downstream at $x/d = 2$. Whereas the simulations

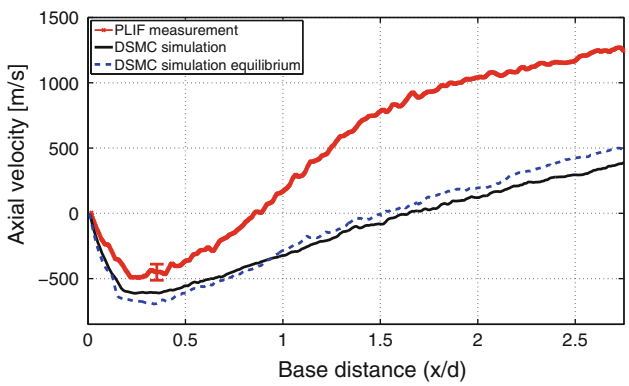

Fig. 8 Axial velocity distribution along the flow centerline. The freestream velocity has been measured at 2,410 m/s

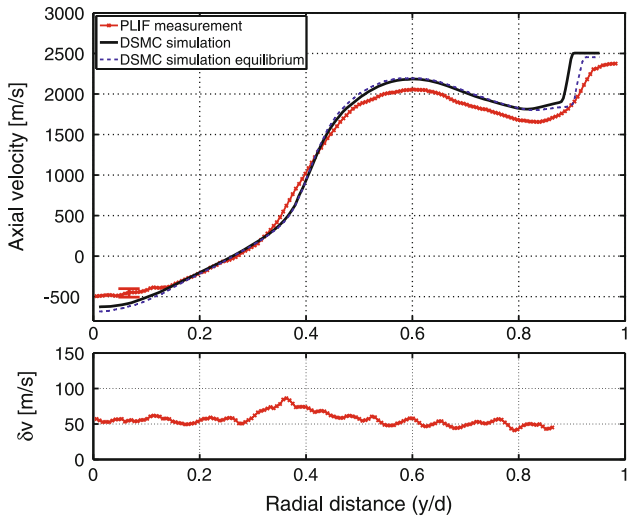

(a) $x/d = 0.25$

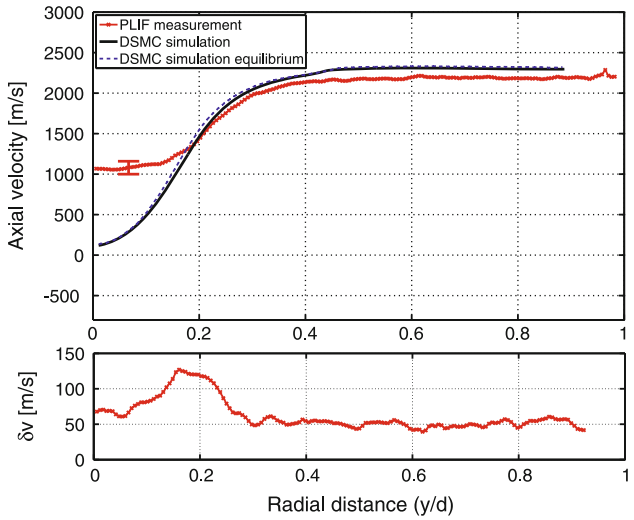

(b) $x/d = 2.0$

Fig. 9 Comparison of axial velocity component in the near and far wake. δv in the lower graph shows the 95% confidence bounds of the measured *absolute* velocity

indicate a distinctive velocity minimum at the flow centerline with large gradients in the radial direction, the measurements show a comparatively constant velocity distribution within the inner wake for radii $y/d < 0.2$. The largest uncertainties of the velocity measurement also occur at this radial location. Increased uncertainty occurs where the flow field shows local unsteadiness (Hruschka et al. 2010).

The differences become particularly obvious when simulated and measured streamlines are compared, as in Fig. 10. In the experiments, the recirculation region is only about half as long as in the simulations, leading to a truncated shape of the recirculation region in the measured case. Despite this discrepancy, the location of the experimental vortex center is well predicted by the simulation.

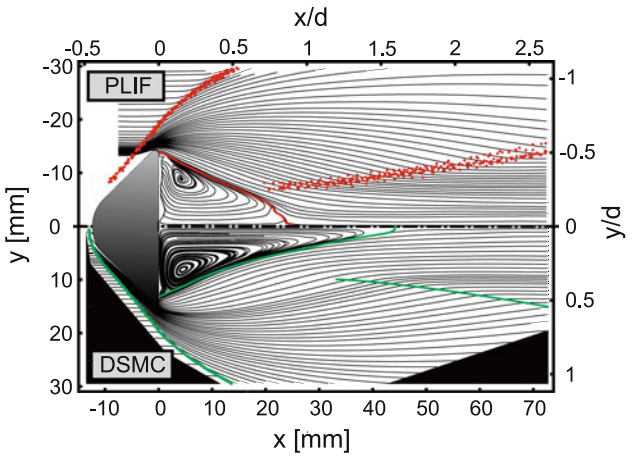

Fig. 10 Streamline plot (PLIF measurement, top and DSMC simulation, bottom). The observed bow and recompression shocks and the dividing streamline are rendered red for the measurement and green for the simulation. The spacing between streamlines has been optimized to illustrate all flow features clearly

Some disagreements near the wall are caused by the difficulty in measuring near the wall.

As Figs. 7 and 9 indicate, the simulated velocities do not change drastically if the flow is modeled in thermal equilibrium. The magnitude of the peak velocity in the recirculation region is about 8% higher in this case.

6.2 Temperature

Measured and simulated rotational temperatures are compared in Fig. 11. In general, simulation and measurement agree well in the inviscid outer wake, where the complexity of the flow field is limited. In this region, the velocity measurement also has shown good agreement with simulations. The temperature jump across the bow shock is also influenced by vibrational relaxation processes, as indicated in Fig. 4. Vibrational relaxation further away from the

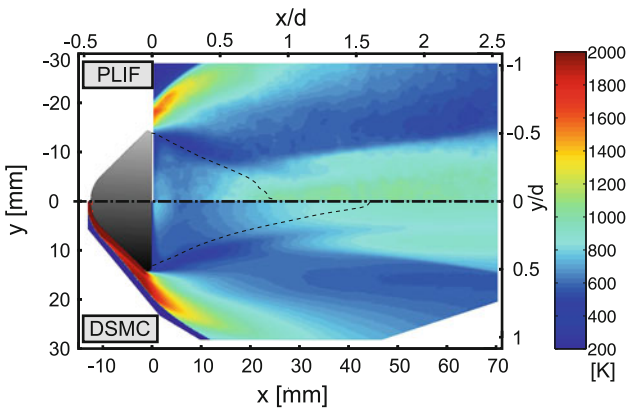

Fig. 11 PLIF rotational temperature measurement (*top*) and DSMC simulation with thermal non-equilibrium (*bottom*). The dividing streamlines are indicated by the *dashed lines*

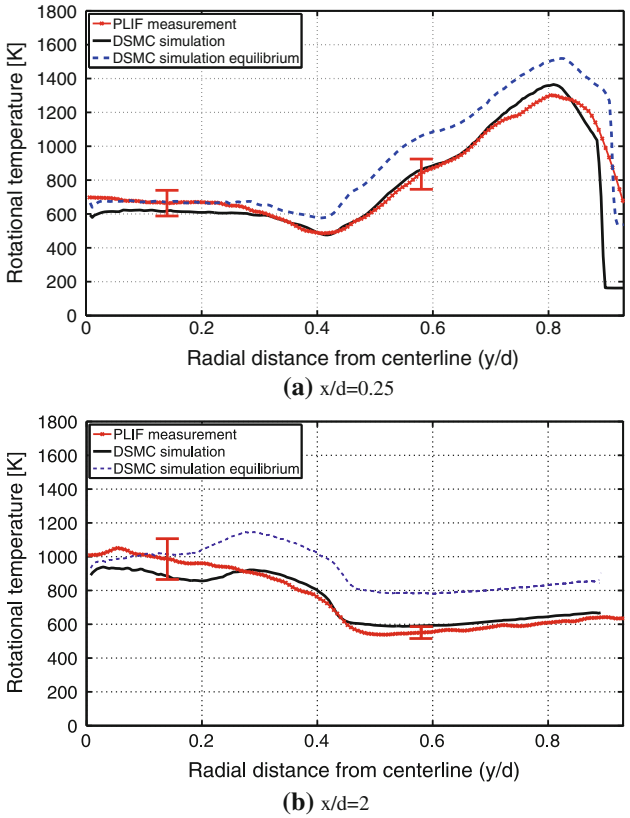

Fig. 12 Comparison of DSMC and PLIF temperatures at different distances from the base

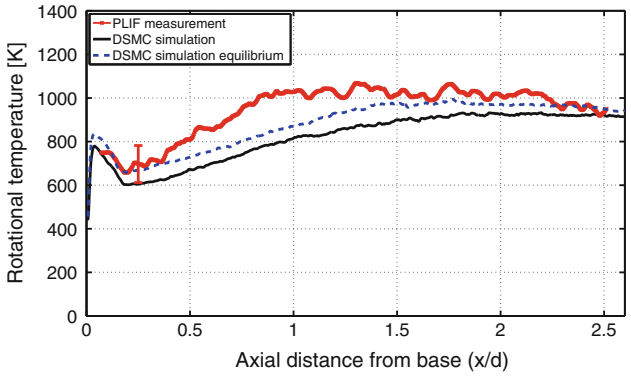

Fig. 13 Temperature along the flow centerline

centerline only occurs to a small extent, as the shock loses strength with distance from the centerline and becomes more oblique. The overall good agreement between simulation and measurement, however, indicates that these relaxation processes are simulated correctly.

Figure 12a, b show the radial temperature distribution in the near and far wake, respectively. At both axial distances, the measured temperatures in the outer wake, where $y/d > 0.35$, agree with the non-equilibrium simulation, while the equilibrium simulation is outside the 95% confidence intervals. In hypersonic flows around blunt bodies, values of T_{vib}/T_{tr} larger than unity typically occur within the expansion after flow separation from the model shoulder (Zhong et al. 2008). This is supported by the current measurements, but as seen in Fig. 4, T_{vib}/T_{tr} is also large in the outer wake and the tunnel free steam, which is not the case for typical atmospheric planetary entry flows, which are in vibrational equilibrium in the freestream (Zhluktov et al. 1996).

Similar to the velocity measurement, the temperature jump across the bow shock (at $y/d \approx 0.9$ in Fig. 12a) is not as sudden as the simulations indicate. Motion blur, local shock unsteadiness, and some additional secondary fluorescence in the F_2 signal, which occurs in the freestream immediately before the flow passes through the bow shock, are responsible for the inaccuracy of the measurement in this region.

The measured temperatures in the inner wake, however, are systematically high when compared with the simulations, a difference that is particularity noticeable at the flow centerline, shown in Fig. 13. The largest discrepancy occurs at the measured location of the rear stagnation point, $x/d = 0.85$. Random measurement uncertainties at the flow centerline are larger than elsewhere in the flow, as discussed in Sect. 5.2. They do not, however, explain the difference entirely, even though faster vibrational relaxation at the centerline could reduce the discrepancy, as indicated by the equilibrium simulation.

7 Transitional effects in the far wake

In the outer wake, simulation results for both velocity and temperature agree well with experimental data. This region is expected to be entirely laminar at the current global Reynolds number Re_d of 3.5×10^4, which is at least two orders of magnitude lower than typical values necessary for transition in the outer wake. Turbulence in the inner wake downstream of the base, however, can occur at Re_d as low as 150 (Lees 1964). The transition from laminar to turbulent flow itself is a gradual process. From incipient transition, i.e. the first occurrence of nonlinearities, disturbances grow with distance downstream of the base. The point where they grow overproportionally is usually quoted as the point of full transition, which also causes radial growth of the inner wake, which can be observed in schlieren visualizations (Slattery and Clay 1962; Pallone et al. 1964; Wilson 1967). Apart from Mach and Reynolds number, the influencing factors for the exact location of incipient and full transition are the level of initial fluctuations in the freestream (Schneider 2001), the bluntness of the body, and to a small extent the body shape and whether the flow is two-dimensional or axisymmetric (Liou et al.

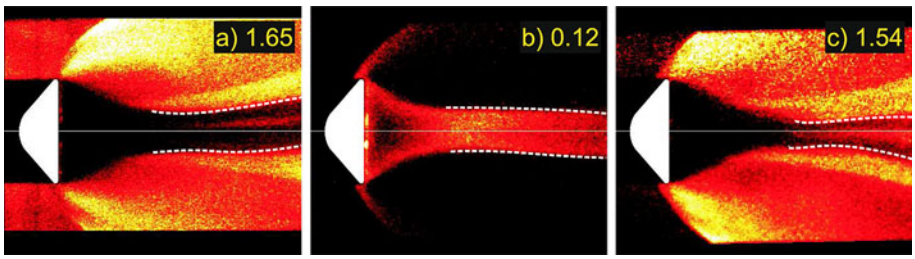

Fig. 14 Some visualizations of the far wake structure, showing sinusoidal motion as a possible precursor to transition, indicated by *white dashed lines*. The pictures look inherently different, as they were taken at different laser detunings from line center (Hruschka et al. 2010), printed in each picture in picometers

1993). Although some theoretical correlations exist (Gold 1963), distances from the base to full transition $(x/d)_{tr}$ are usually estimated using empirical correlations, such as that of Lees (1964). The experimental data used by Lees suggest a linear relation between $(Re_{f,d})^{-1}$ and $(x/d)_{tr}$ (derived from Lees (1964)):

$$(x/d)_{tr} = 5.57 \times 10^4 / Re_{f,d} \quad (4)$$

where $Re_{f,d}$ is the local wake edge Reynolds number (Webb et al. 1963) at the inviscid outer radius of the inner wake, where temperature, velocity and density, and hence $Re_{f,d}$ are comparatively constant. The simulations, which agree with the measurements at this location, provide a value for $Re_{f,d}$ of approximately 4,500. Using this value in Eq. 4 allows one to estimate $(x/d)_{tr} \approx 12$ for the current flow field. This lies outside the field of view of the current measurements, so full transition should not be observed in either the current PLIF measurements or in time-resolved resonantly enhanced shearing interferometry visualizations (Hruschka et al. 2008) conducted at a similar flow condition (Hruschka et al. 2009). Precursors to full transition, however, occur further upstream and are most likely not only responsible for the discrepancies between simulation and measurements but also for the typical radial distribution of measurement uncertainty caused by local flow unsteadiness in the far wake, shown earlier in Fig. 9b. A characteristic feature of these velocity fluctuations within wakes prior to full transition is that they have a local minimum at the centerline, as reported by Behrens (1968) for a cylinder, Behrens and Ko for a flat plate (Behrens et al. 1971), and Demetriades for a wedge (1964) and for an axisymmetric wake (Demetriades 1967). These fluctuations originate close to the location of the recompression shock and usually grow with downstream distance and were also observed in some shadowgraph visualizations (Venkatapathy et al. 1991). The localized disturbances cause increased mixing and fluid entrainment from the recirculation region into the free shear layer. The resulting loss of momentum shortens the recirculation region when compared with simulations, which is responsible for its truncated appearance in Fig. 10. The velocity distribution for radial locations $y/d < 0.2$ is comparatively constant, and the velocity deficit at the centerline is smaller than simulated, as plotted in Fig. 9b. The comparison shows similarity to the DSMC comparison by Zhong et al. (Zhong et al. 2008) with the axisymmetric wake velocity profiles of Murman (1969). Also, the slender body flow at Mach 16 and $Re_d = 1.2 \times 10^5$ investigated in (Murman 1969) is expected to show full transition at a similar value for $(x/d)_{tr}$ to the current flow (Waldbusser 1967). The smaller centerline velocity deficit in the experiments compared to the simulations, which remain laminar, is typically observed in transitional or turbulent flows, as demonstrated in the wake pitot pressure maps of both laminar and turbulent flow around a cylinder, measured by McCarthy and Kubota (1964). According to Muntz and Softley (1966), the position of peak temperature coincides approximately with that of the rear stagnation point, which in our experiments is found closer to the base than in the simulations. This probably accounts for most of the difference of up to 25% at the centerline between measured and simulated temperatures, shown in Fig. 13. The temperature difference at the measured and simulated rear stagnation points, however, is only $\approx$10% and could also be due to random error, or possibly faster vibrational relaxation than modeled in the thermal non-equilibrium simulation.

Apart from increased fluctuations in measurement signals, other observable precursors of transition are sinusoidal instabilities (Gold 1963), which can occur in axisymmetric wakes. They were observed not only in the schlieren visualizations of e.g. Wilson (1967) or Pallone et al. (1964), but also in some of the PLIF flow visualizations in the current study, shown in Fig. 14. These oscillations typically occur at lower frequencies compared to the characteristic frequencies of the fluctuations observed at $y/d \approx 0.2$, which play a key role in the transition to full turbulence further downstream (Behrens and Ko 1971).

An overview of measured and simulated inner wake properties is given in Table 5. Results obtained with a commercial NS-based equilibrium CFD code (Metacomp Technologies 2007), described in Hruschka (2010), are also

Table 5 Summary of measurement and simulation results: axial freestream velocity ($V_{\infty,=}$), radial freestream velocity at $y/d = 1$ ($V_{\infty,\perp}$), peak reverse flow velocity ($V_{R,max}$), position of rear stagnation point ($(x/d)_{RSP}$), minimum temperature at the centerline ($T_{R,min}$) and base pressure (p_B)

Line/method	$V_{\infty,=}$ [ms]	$V_{\infty,\perp}$ [ms]	$V_{R,\max}$ [ms]
Measurement	2,410 ± 50	53 ± 50	492 ± 50
DSMC	2503*	57*	612
DSMC (EQI.)	2503*	57*	660
CFD (EQI.) (Hruschka 2010)	2503*	57*	810
Line/method	**$(x/d)_{RSP}$ [−]**	**$T_{R,\min}$ [K]**	**p_B [Pa]**
Measurement	0.85 ± 0.03	656 ± 85	500 ± 100
DSMC	1.64	600	565
DSMC (EQI.)	1.65	660	807
CFD (EQI.) (Hruschka 2010)	1.67	750	983

* Input values from nozzle code

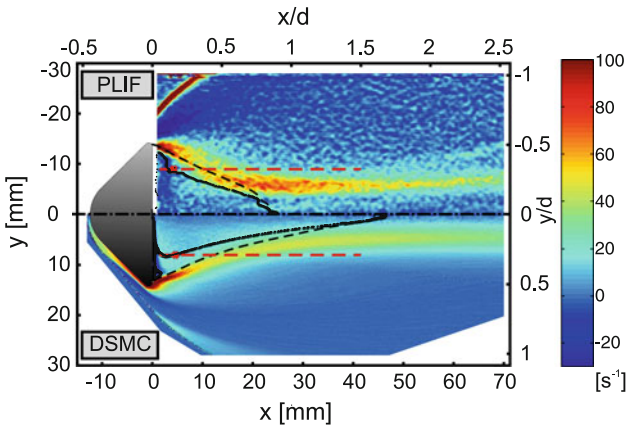

Fig. 15 Near-wake vorticity map. The upper half is obtained from the measured velocity and the lower half from the simulation. The *red crosses mark* the position of the vortex core. Dividing streamlines (*black dashed line*) and zero-axial-velocity-locations (*black markers*) are superimposed

listed. The relatively large uncertainty of the measured base pressure includes possible errors due to slightly different conditions (Park 2009) for the measurement of p_B. The measured value, however, agrees with the non-equilibrium simulation within uncertainties but not with the equilibrium simulation. Enforcing thermal equilibrium leads to higher relaxation rates in the shoulder expansion, higher inner wake temperatures, and thus higher base pressures than in the simulated non-equilibrium case.

8 Vorticity comparison

The vorticity distribution in the near wake is an important derived quantity, because it describes the motion of the vortex immediately downstream of the body. The type of the vorticity distribution has been assumed in a number of analytical descriptions of the near-wake flow in previous investigations. The first model was proposed by Chapman et al. (1965) and treated the recirculating region as a stagnant gas and assumed that the boundary layer at separation had zero thickness. Denison and Baum (1963) extended the model to a finite initial thickness, and this idea has formed the basis of several popular predictions of base pressure for these flows. Batchelor (1956) considered the case of vortices at high Reynolds number, treating them as a region of solid-body rotation surrounded by the boundary layer on the body, the separated shear layer, and the recirculating flow near the axis, and driven by the viscous stresses in the shear layer. Weiss (1966) investigated the applicability of this model to slender bodies in hypersonic flow and concluded that even at length-based freestream Reynolds numbers of 10^6, the recirculation should be fully viscous, with the boundary layer on the base making up approximately one-third of the base diameter, which questions the validity of Batchelor's thin-layer model for high-Reynolds-number wake flows. More recently, Grasso and Pettinelli (1995) have performed Navier-Stokes-based simulations on wake flows, considering the effects of Mach number, Reynolds number, and forebody shape on the character of the wake. This study characterized the vorticity behavior in the near wake as a function of the Reynolds number along the dividing streamline, $Re_{ds,d}$. Using the base diameter as a reference, Grasso and Pettinelli found that for $Re_{ds,d} \leq 200$, the vorticity increases linearly from the core outwards to the driving shear layer. They termed this behavior as 'diffusive'. For $200 \leq Re_{ds,d} \leq 1{,}000$, the behavior changes from diffusive to solid-body rotation. The latter is referred to as 'convective behavior' by Grasso and Pettinelli and purely convective behavior at higher values of $Re_{ds,d}$, with $Re_{ds,d} > 2{,}000$ generating a secondary vortex below the separation point. Based upon the simulated flow conditions, the dividing streamline Reynolds number is $Re_{ds,d} \approx 1{,}000$, so according to the findings of Grasso and Pettinelli, the vortex in these experiments should be convective.

Figure 15 shows a map of the vorticity for the simulated and measured velocity fields, with the measured field in the upper half of the image and the simulated field in the lower half. The vorticity reaches a maximum in the shear layer in both cases and thus shows the extent of the shear layer very clearly. It is also clear from Fig. 15 that the measured recirculation region is much smaller in size than the simulated region, while the peak vorticity region within the shear layer is about twice as thick for the experiment as it is for the simulation. The peak vorticity value is similar for both the measured and simulated cases; however, experimental values at $x/d \approx 1$ and $y/d \approx 0.2$ are higher. In the

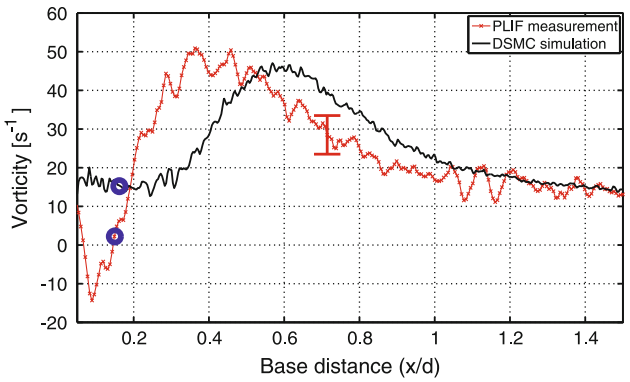

Fig. 16 Vorticity along a horizontal line through the vortex core, marked as a *red dashed line* in Fig. 15. The position of the vortex core is marked by a *blue circle*

far wake, regions of high vorticity at $y/d \approx 0.2$ coincide with regions of high flow unsteadiness and hence velocity error, as shown previously in Fig. 9b.

Figure 16 is a plot of the vorticity along a horizontal line through the core of the vortex for each of the two fields in Fig. 15. The plot begins at $x/d = 0.05$, because the PLIF measurement is affected by laser scatter at locations nearer to the base. Because the vorticity is derived from the measured velocity, uncertainty propagation causes the experimental vorticity to vary by approximately ± 5 s^{-1} about the mean value. The vortex core is located at $x/d = 0.16$ and $y/d = 0.28$ for the simulations, while for the experimental data, the core is located at $x/d = 0.15$ and $y/d = 0.31$. As the plot shows, the simulated vorticity is relatively constant between 0.05 and 0.35 base diameters downstream of the model base, indicating a convectively driven vortex. This is consistent with the behavior predicted by Grasso and Pettinelli for $Re_{ds,d} = 1000$. There is, however, a significantly different behavior in the experimental vorticity plot. In this case, the vorticity is near zero between $0.05 < x/d < 0.2$, but then linearly increases to 50 s^{-1} in the middle of the shear layer at $x/d = 0.35$. The two plots show qualitatively similar reductions in vorticity downstream of the peak value, although this occurs further downstream for the simulated flow.

The fact that the measured vorticity is nearly zero in the vicinity of the vortex core indicates that the central part of the vortex is close to Chapman's assumption of a 'dead air' region. The linear increase in vorticity between $0.02 < x/d < 0.35$ indicates a more Stokes-like diffusive flow. One possible reason for this discrepancy relates to the incipient transition in the shear layer discussed previously. Transition from laminar to turbulent flow is not predicted in our DSMC simulations, and Grasso and Pettinelli's Navier-Stokes-based computations assume laminar flow. If transition is occurring in the free shear layer, the mixing in the shear layer will be stronger than in the laminar case, and the velocity profile in the shear layer will be fuller than for the laminar shear layers predicted in the simulations. This uncertainty would have the effect of reducing both the driving force on the vortex and the Reynolds number of the vortex flow, producing behavior consistent with that of the measured vorticity plot in Fig. 16.

9 Conclusions

A non-reacting, hypersonic wake flow generated by a shock tunnel has been investigated by means of experiment and simulation. Velocity was measured within uncertainties of approximately ± 50 m/s whereas temperature could be measured within ± 70–150 K. To the authors' knowledge, this is the first global measurement of velocity and temperature in a wake flow without the compromise of stings or sensor intrusions and provides the first experimental vorticity map in one of these flows.

Good agreement with simulation in the outer wake was found, as in this region, the flow can be considered inviscid. The exclusive agreement of the rotational temperature with a simulation modeling realistic thermal relaxation highlights the importance of modeling thermal non-equilibrium in these flows. If the vibrational freezing in the expansion at separation was not accounted for, the results for temperature and to a smaller extent velocity would be compromised, and in addition those for surface properties at the base, as Table 5 shows.

The largest discrepancy between simulation and measurement was found in the inner far wake. Distributions of fluctuations in the measurement signal typical for wake flows upstream of full transition to turbulence were observed, amongst other indicators such as sinusoidal instabilities. Empirical correlations from the literature indicate that full transition of the flow occurs downstream of the field of view, but the measurements point to the effect of incipient transition on the wake. This is particularly obvious for the shape of the recirculation region, which is only half as long in the experimental case as it is for the simulation. Similarly to earlier investigations, the experimentally determined velocity deficit at the centerline is smaller than in the simulation. Analysis of the sensitive and non-intrusive PLIF technique assures that the discrepancy cannot be explained by random uncertainty or bias error. The velocity measurements also show that the effects of incipient transition are much more obvious in the far wake behind recompression, whereas velocity and temperature in the near wake are still comparatively similar to the perfectly laminar simulation. The effect of incipient transition on base pressure is also small, compared to the influence of the modeling of thermal relaxation.

The higher measured temperature when compared with simulations approximately one model diameter downstream of the base could be an important consideration for the design of planetary entry vehicles, particularly when heat-sensitive payloads are present in this region.

Comparison between the computed vorticity field and that derived from the measured velocity also shows a qualitative difference in the vortex behavior, with the experiments indicating a diffusive vorticity distribution where computations indicate that the vortex should undergo solid-body rotation. This discrepancy is most likely caused by the better mixing caused by the velocity fluctuations in the shear layer in the experiment, which provides less of a driving force to the vortex than would be expected for a purely laminar flow.

The freestream fluctuations produced by a shock tunnel facility can promote transition in the shear layer (Schneider 2001). At the current stage, the noise level of the T-ADFA shock tunnel cannot yet be fully quantified; hence, it has not been included in the simulations. Our results suggest, however, that fluctuating parameters in inlet conditions should be modeled as well to produce better fidelity in computational simulations of these flows.

Acknowledgments This work was funded by the Australian Research Council under discovery project DP0666941. We thank G. Foppoli and P. Walsh for their technical support. The contributions of G. Park, S. Gai and K. Watts are appreciated. Furthermore, we would like to acknowledge the courtesy of G. A. Bird for letting us use his DS2V (V4.5) DSMC code.

References

Batchelor GK (1956) A proposal concerning laminar wakes behind bluff bodies at large Reynolds number. J Fluid Mech 1:177–190

Beck WH (1999) Spectroscopic techniques for measurement of velocity and temperature in the DLR high enthalpy shock tunnel HEG. In: RTO AVT Course on "Measurement Techniques for High Enthalpy and Plasma Flows", held in Rhode-Saint-Genese, Belgium

Behrens W (1968) Far wake behind cylinders at hypersonic speeds: II. Stability. AIAA J 6(2):225–228

Behrens W, Ko DRS (1971) Experimental stability studies in wakes of two-dimensional slender bodies at hypersonic speeds. AIAA J 9(5):851–857

Bird GA (1994) Molecular gas dynamics and the direct simulation of gas flows. Clarendon Press, Oxford

Bird GA (2007) Sophisticated DSMC. Notes prepared for a short course at the DSMC07 meeting, Santa Fe, New Mexico

Borgnakke C, Larsen PS (1975) Statistical collision model for Monte Carlo simulation of polyatomic gas mixture. J Comput Phys 18(4):405–420

Boyd ID, Chen G, Candler GV (1995) Predicting failure of the continuum fluid equations in transitional hypersonic flows. Phys Fluids 7(1):210–219

Chapman DR, Kuehn DM, Larson HK (1958) Investigation of separated flows in supersonic and subsonic streams with emphasis on the effect of transition. Tech. Rep. NACA-report-1356, Ames Aeronautical Laboratory

Danckert A, Legge H (1996) Experimental and computational wake structure study for a wide-angle cone. J Spacecraft Rockets 33(4):476–482

Danehy PM, Mere P, Gaston MJ, O'Byrne S, Palma PC, Houwing AFP (2001) Fluorescence velocimetry of the hypersonic separated flow over a cone. AIAA J 39:1320–1328

Danehy PM, O'Byrne S, Houwing AFP, Fox JS, Smith DR (2003) Flow-tagging velocimetry for hypersonic flows using fluorescence of nitric oxide. AIAA J 41(2):263–271

Demetriades A (1964) Hot-wire measurements in the hypersonic wake of slender bodies. AIAA J 2(2):245–250

Demetriades A (1967) Turbulent fluctuation measurements in compressible, axisymmetric wakes. AIAA J 5(5):1028–1029

Demtröder W (1999) Laserspektroskopie, 4 edn. Springer, Berlin

Denison MR, Baum E (1963) Compressible free shear layer with finite initial thickness. AIAA J 1(2):342–349

Dewey CF (1965) Near wake of a blunt body at hypersonic speeds. AIAA J 3(6):1001–1010

Dogra VK, Moss JN, Wilmoth RG, Taylor JC, Hassan H (1995) Effects of chemistry on blunt-body wake structure. AIAA J 33(3):463–469

Earls LT (1935) Intensities in $^2\Pi - ^2\Sigma$ transitions in diatomic molecules. Phys Rev 48:423–424

Eckbreth AC (1996) Laser diagnostics for combustion temperature and species, 2 edn. Gordon and Breach Publishers, Amsterdam

Gai SL (1992) Free piston shock tunnels: development and capabilities. Prog Aerospace Sci 29(1):1–41

Gnoffo PA (1999) Planetary-entry gas dynamics. Ann Rev Fluid Mech 31:459–494

Gold H (1963) Stability of laminar wakes. Ph.D. thesis, California Institute of Technology, Pasadena, California

Grasso F, Pettinelli C (1995) Analysis of laminar near-wake hypersonic flows. J Spacecraft Rockets 32(6):970–980

Hornung HG, Lemieux P (2001) Shock layer instability near the Newtonian limit of hypervelocity flows. Phys Fluids 13(8): 2394–2402

Houwing AFP, Palmer JL, Thurber MC, Wehe SD, Hanson RK, Boyce RR (1996) Comparison of planar fluorescence measurements and computational modelling of shock-layer flow. AIAA 34(3):470–477

Hruschka R, O'Byrne S, Kleine H (2008) Diode-laser-based near-resonantly enhanced flow visualisation in shock tunnels. Appl Opt 47(24):4352–4360

Hruschka R, O'Byrne S, Kleine H (2010) Two-component Doppler-shift fluorescence velocimetry applied to a generic planetary entry probe model. Exp Fluids 48(6):1109–1120

Hruschka R, Park G, O'Byrne S, Kleine H (2009) Optical investigation of transient phenomena in hypersonic shock tunnels. In: Proceedings of SPIE, volume 7126, 28^{th} international congress on high-speed imaging and photonics, Canberra, Australia, November 2008

Hruschka RB (2010) Optical studies and simulations of hypervelocity flow fields around blunt bodies. Ph.D. thesis, University of New South Wales at the Australian Defence Force Academy, School of Engineering and Information Technology

Inger GR, Moss JN (2007) Comparison of Navier-Stokes and direct simulation Monte Carlo predictions with separation. AIAA J 45(8):2102–2105

Lees L (1964) Hypersonic wakes and trails. AIAA J 2(3):417–528

Liou WW, Fang Y, Bird GA (1993) DSMC simulations of forced chaotic flows. In: AIAA Paper, pp 1993–3595

Lofthouse AJ, Boyd ID, Wright MJ (2007) Effects of continuum breakdown on hypersonic aerothermodynamics. Phys Fluids 19(2):027, 105

Lofthouse AJ, Scalabrin LC, Boyd ID (2008) Velocity slip and temperature jump in hypersonic aerothermodynamics. J Thermophys Heat Trans 22(1):38–49

Metacomp Technologies (2007) CA 91301, USA: CFD++ (http://www.metacomptech.com)
McCarthy JF Jr, Kubota T (1964) A study of wakes behind a circular cylinder at M = 5.7. AIAA J 2(4):629–636
McIntosh MK (1968) Computer program for the numerical calculation of frozen and equilibrium conditions in shock tunnels. Tech. rep., Australian National University
McIntyre TJ, Bishop AI, Thomas AM, Sasoh A, Rubinsztein-Dunlop H (2000) Ionizing nitrogen and air flows in a superorbital expansion tube. AIAA J 38(9):1685–1691
McMillin BK (1993) Instantaneous two-line PLIF temperature imaging of nitric oxide in supersonic mixing and combustion flowfields. Ph.D. thesis, Stanford University, Department of Mechanical Engineering
Mitcheltree RA, DiFulvio M, Horvath TJ, Braun RD (1999) Aerothermal heating predictions for Mars Microprobe. J Spacecraft Rockets 36(3):405–411
Moss JN (2007) Direct simulation Monte Carlo simulations of ballute aerothermodynamics under hypersonic rarefied conditions. J Spacecraft Rockets 44(2):289–297
Moss JN, Bird GA (2005) Direct simulation Monte Carlo simulations of hypersonic flows with shock interactions. AIAA J 43(12):2565–2573
Moss JN, Price JM (1997) Survey of blunt body flows including wakes at hypersonic low-density conditions. J Thermophys Heat Trans 11(3):321–329
Muntz EP, Softley EJ (1966) A study of laminar near wakes. AIAA J 4(6):961–968
Murman EM (1969) Experimental studies of a laminar hypersonic cone wake. AIAA J 7(9):1724–1730
O'Byrne S (2002) Hypersonic laminar boundary layers and near-wake flows. Ph.D. thesis, Department of Physics, Australian National University
O'Byrne S, Danehy PM, Houwing AFP (2006) Investigation of hypersonic nozzle flow uniformity using NO fluorescence. Shock Waves 15(2):81–87
Ozawa T, Zhong J, Levin DA (2008) Development of kinetic-based energy exchange models for noncontinuum, ionized hypersonic flows. Phys Fluids 20(046102):1–18
Pallone A, Erdos J, Eckermann J (1964) Hypersonic laminar wakes and transition studies. AIAA J 2(5):855–863
Park G, Hruschka R, Gai S, Neely A (2009) Flow establishment behind blunt bodies at hypersonic speeds in a shock tunnel. In: Proceedings of SPIE, Volume 7126, 28th International Congress on High-Speed Imaging and Photonics, Canberra, Australia, November 2008
Reeves BL (1965) Theory of laminar near wake of blunt bodies in hypersonic flow. AIAA J 3(11):2061–2074
Ruffin SM (1993) Vibrational relaxation times in expanding flows. J Spacecraft Rockets 30(1):59–68
Schneider SP (2001) Effects of high-speed tunnel noise on laminar-turbulent transition. J Spacecraft Rockets 38(3):323–333
Schwarzentruber TE, Scalabrin LC, Boyd ID (2008) Hybrid particle-continuum simulations of nonequilibium hypersonic blunt-body flowfields. J Thermophys Heat Trans 22(1):29–37
Seitzman JM, Hanson RK (1993) Planar fluorescence imaging in gases, chap 6. Academic Press, London
Shen C (2005) Rarefied gas dynamics—fundamentals, simulations and micro flows, 1 edn. Springer, Berlin
Slattery RE, Clay WG (1962) Laminar-turbulent transition and subsequent motion behind hypervelocity spheres. ARS J 32:1427–1429
Sohn I, Ozawa T, Levin DA, Modest MF (2009) DSMC hypersonic reentry flow simulations with photon Monte Carlo radiation. In: AIAA Paper, pp 2009–1566
Todisco A, Pallone AJ (1965) Near wake flow field measurements. AIAA J 3(11):2075–2080
Venkatapathy E, Palmer G, Prabhu DK (1991) AFE base flow computations. In: AIAA Paper, pp 1991–1372
Waldbusser E (1967) Shape effects on hypersonic slender body wake geometry and transition distance. J Spacecraft Rockets 4(5):657–662
Webb WH, Hromas L, Lees L (1963) Hypersonic wake transition. AIAA J 1(3):719–721
Weiss RF (1966) Base pressure of slender bodies in laminar, hypersonic flow. AIAA J 4(9):1557–1559
Wilson LN (1967) Far wake behavior of hypersonic spheres. AIAA J 5(7):1238–1944
Zakkay V, Cresci RJ (1966) An experimental investigation of the near wake of a slender cone at $M_\infty = 8$ and 12. AIAA J 4(1):41–46
Zhluktov SV, Utyuzhnikov SV, Tirsky GA (1996) Numerical investigation of thermal and chemical nonequilibrium flows past slender and blunted cones. J Thermophys Heat Trans 10(1):137–147
Zhong J, Ozawa T, Levin DA (2008) Comparison of high-altitude hypersonic wake flows of slender and blunt bodies. AIAA J 46(1):251–262